Extended Absorption Window and Improved Stability of Cesium-Based Triple-Cation Perovskite Solar Cells Passivated with Perfluorinated Organics

K. M. Muhammed Salim,[†] Teck Ming Koh,[†] Damodaran Bahulayan,[†] P. C. Harikesh,[‡] Nur Fadilah Jamaludin,[‡] Benny Febriansyah,[†] Annalisa Bruno,[†Δ] Subodh Mhaisalkar,[†§] and Nripan Mathews[†§]*

[†]Energy Research Institute @ NTU (ERI@N), Research Techno Plaza, X-Frontier Block, Level 5, 50 Nanyang Drive, Singapore 637553

[‡]Interdisciplinary Graduate School, Nanyang Technological University, 50 Nanyang Avenue, Singapore 639798

[Δ]Division of Physics and Applied Physics, School of Physical and Mathematical Sciences, Nanyang Technological University, 21 Nanyang Link, Singapore 637371

[§]School of Materials Science and Engineering, Nanyang Technological University, 50 Nanyang Avenue, Singapore 639798

Corresponding Author

*Email: Nripan@ntu.edu.sg

ABSTRACT: Despite the high-quality films achieved with triple cation perovskites, the deviation from optimized band gap by virtue of Shockley-Queisser estimation signify consequential light absorption losses in this system. Herein, it is shown that, by passivating the perovskite surface with a hydrophobic fluorinated organic salt namely pentafluoropropylamonium iodide (PFPAI), not only is the band gap narrowed, the process also contributes towards the modulation of surface and electronic properties of the resulting film. Cumulative effect of these factors promotes the enhancement in power conversion efficiency (PCE) and moisture stability of the perovskite solar cells (PSCs) fabricated with the PFPAI passivated films. Suppression of surface defects and mitigation of interfacial charge recombination in the treated film are in good agreement with the longer photoluminescence (PL) decay lifetime observed. The PFPAI-passivated PSC afforded a PCE of 16.6 % with good ambient stability, evidenced by minimal change in normalized PCE on storage in a relative humidity (RH) environment of 55% over a period exceeding 169 days.

TOC GRAPHICS

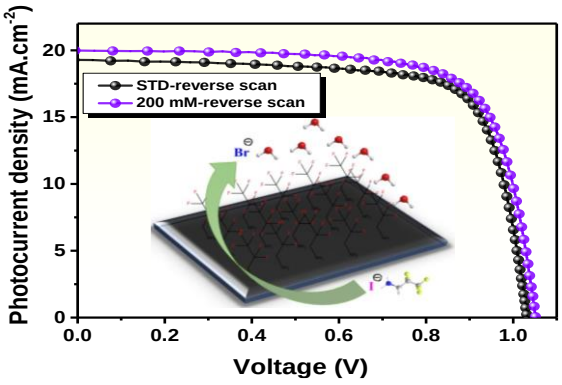

Hybrid organic-inorganic perovskites (HOIPs) with the ABX_3 composition [A = Cs^+ (cesium), $CH_3NH_3^+$ (methylammonium, MA), or $NH{=}CHNH_3^+$ (formamidinium, FA); B = Pb^{2+}; X = Br, I] have been identified as an emerging class of light harvesters[1-2] owing to the stellar optoelectronic properties such as high absorption coefficients,[3-4] tunable band gap,[4-9] low exciton binding energies,[10] good charge carrier mobility[11-13] and long charge carrier diffusion lengths (in the μm range)[11-16] accessible through a low-cost solution-based process. It is thus unsurprising that HOIP solar cells have charted record efficiencies within a few years.[4, 17-19] The versatility offered by this unique class of semiconductors has paved the way for their implementation in applications beyond photovoltaics, such as lasing,[20-22] light-emitting diodes,[23-25] photodetectors,[26-27] X-Ray detectors,[28] and field-effect transistors.[29]

Although numerous perovskite analogs have been reported, research into this class of materials has been largely focused on methylammonium lead iodide ($MAPbI_3$) due to its optimum band gap of 1.55 eV for solar cell applications. Formamidinium (FA) provides a promising alternative to $MAPbI_3$ due to its enhanced light absorption through the lower band gap of 1.48 eV.[30] Recent efforts have focused on a system consisting of highly efficient double cation perovskites (MA/FA) with the addition of an inorganic cation cesium (Cs). More commonly known as the "triple"[31] system due to the use of a cation pool, it offers high power conversion efficiency, extended moisture, and thermal stability. The salient features of this system stem from the suppression of photo inactive δ-phase of $FAPbI_3$ and subsequent formation of highly uniform perovskite grains through seed-assisted crystal growth. Thermally stable and more robust towards varying fabrication conditions, the triple-cation system provides a higher degree of reproducibility as compared to its single cation $MAPbI_3$ and $FAPbI_3$ counterparts. However, its band gap (1.64 eV) is broader than $MAPbI_3$ and $FAPbI_3$ due to the presence of bromide ions which could potentially

constrain the light absorption. Besides the non-ideal bandgap, halide perovskite thin films also display higher surface defect densities,[32-33] necessitating the development of surface passivation for alleviating non-radiative charge recombination at the interfaces.[34-35] Previous attempts have included the treatment of perovskites with π-conjugated systems such as porphyrin,[36] thiol-functionalized molecules,[37] and Lewis base molecules.[38] Thus there is a need for a multi-functional surface passivator which can not only abate surface traps, but also offers improved light harvesting ability and stability.

Herein, we report a surface passivation approach using a hydrophobic fluorinated organic salt; pentafluoropropyl ammonium iodide (PFPAI), to narrow the band gap of triple-cation perovskite through halide substitution. The simultaneous alteration to its surface and electronic properties further enhances the moisture stability and power conversion efficiency (PCE) of the triple-cation perovskite solar cells. The surface passivated perovskite solar cells exhibited notable enhancement of PCE from 14.8% (control) to 16.6% with enhancement across all photovoltaic parameters. The surface passivated cells also showed remarkable stability for more than 169 days under ambient conditions with an average relative humidity (RH) of 55% with no observable change in initial PCE values. In addition, the PFPAI could effectively passivate perovskite surface and grain boundaries as evidenced by the longer photoluminescence (PL) lifetime for the treated films.

The triple-cation perovskite films were prepared with a single-step solvent engineered deposition process similarly to that reported in the literature.[31] It was noted that excess lead iodide in the perovskite precursor solution is beneficial for device performance as reported earlier.[39-41] The detailed procedure adopted for thin film and the device fabrication are detailed in the Experimental Section (Supporting Information). The perovskite films are first prepared on mesoporous TiO_2 prior to spin coating of different concentrations of PFPAI in IPA (50, 100, 200,

500 and 1000 mM) as shown in **Figure 1a.** The films were then subjected to thermal annealing during which color of the perovskite film varied with PFPAI concentration (**Figure S1a)**. As shown in **Figure 1a**, the PFPAI salt contains three carbon atoms tethered with hydrophobic fluorine atoms ($CF_3CF_2CH_2$-) and an ammonium cation (-NH_3^+). During the annealing process; the ammonium group (-NH_3^+) of PFPAI will anchor to the surface of lead octahedron units by means of non-covalent hydrogen bonding interaction. The PFPAI molecules co-ordinate only on the surface of perovskite layer without diffusing to the bulk and allow the complete passivation as well as protection from moisture. In order to verify the increased hydrophobicity expected with PFPAI treatment, the water contact angle test for the standard and 200 mM PFPAI treated perovskite films were carried out (**Figure S2)**. The average contact angle for the film treated with PFPAI concentration of 200 mM film was 66.2°, higher than the 57.1° observed for the standard film. The marked difference in contact angle confirms that surface treatment with hydrophobic PFPAI increases perovskite's moisture resistance.

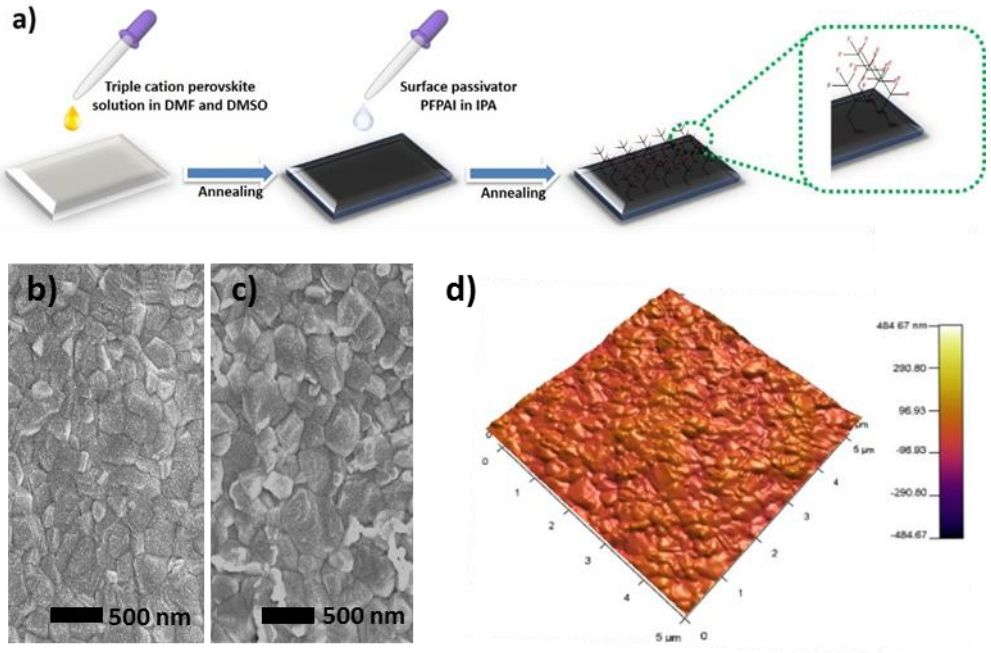

Figure 1. **a) Schematic drawing of PFPAI deposition on perovskite film. Surface morphology image of perovskite film b) standard c) treated with 200 mM PFPAI. d) A topological view of perovskite film treated with 200 mM PFPAI. The scanned area is 5 x 5 μm^2.**

The PFPAI treated perovskite films showed larger perovskite crystallites with lower surface roughness as compared to the standard triple-cation film (**Figure S3**). As shown in **Figure 1b,c** and **Figure S3**, film treated with 200 mM PFPAI exhibited dense uniform perovskite crystallites with grain sizes in the range of 200-400 nm. From **Figure 1d**, the film treated with 200 mM PFPAI was also found to give lower surface roughness (12 nm) as compared to the standard (18 nm). **Figure S4** shows a comparison of the top-view images of the standard and PFPAI treated films imaged using field emission scanning electron microscope (FESEM). Smaller perovskite crystallites with high grain boundary density were observed for the control films whereas treatment with concentrations of PFPAI up to 200 mM afforded pin-hole free films consisting of larger perovskite crystallites. However, on a further increase of PFPAI concentration beyond 200 mM, the films became rough and smaller sized perovskite crystallites with pinholes were observed.

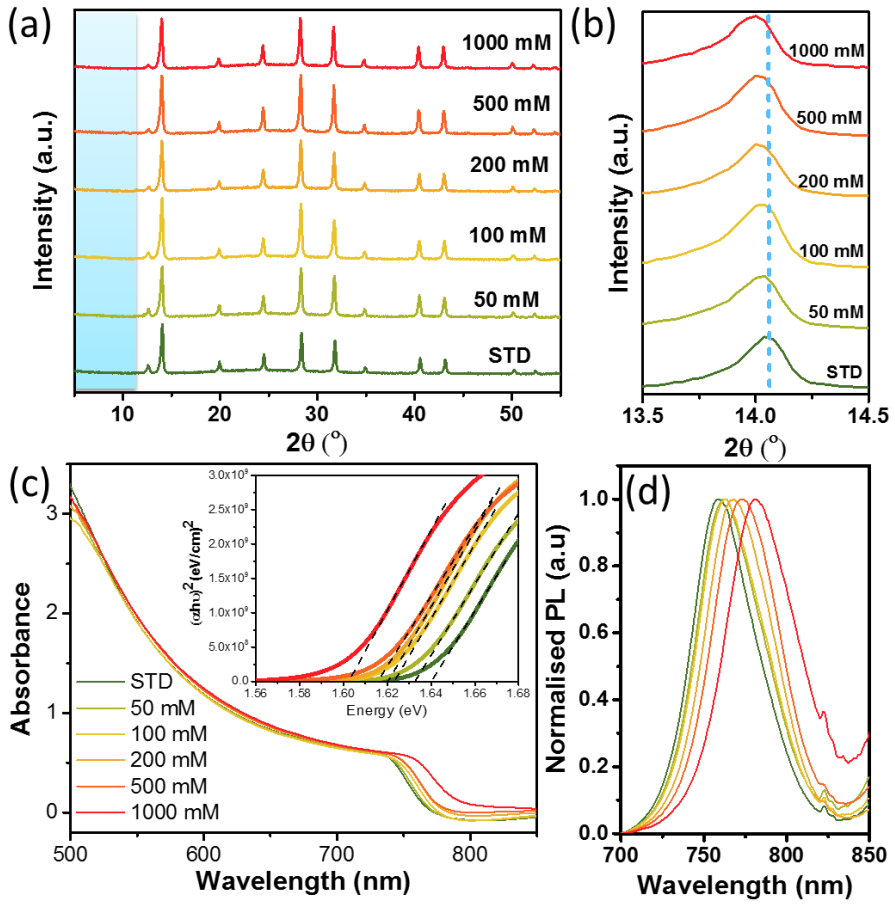

Figure 2. a) Thin film X-ray diffraction pattern of the standard and PFPAI treated films. b) Magnified (110) peak of the standard and PFPAI treated films. c) Normalized UV-Vis absorbance spectra, (inset: Tauc plots). d) Normalized PL spectra.

The X-ray diffraction (XRD) patterns of the standard and PFPAI treated films are shown in **Figure 2a**. Both the surface passivated and the standard triple-cation films showed similar diffraction patterns, confirming that the intrinsic perovskite crystalline phase remains unchanged despite the PFPAI treatment. However, as shown in **Figure 2b** a significant shift in the position of the XRD peaks towards lower angles was observed upon an increase in PFPAI concentration. This is a clear manifestation of unit cell expansion in the perovskite lattice framework by substitution of the smaller bromide ions by larger iodide ions into the perovskite lattice structure. There was no significant diffraction peak observed at 11.7° corresponding to the characteristic peak of δ-

phase $FAPbI_3$. We also noticed a small side peak at 12.71° for all the characterized films attributable to remnant PbI_2 which does not impede the final device performance.[39-41] Similarly, the surface passivated films did not show any diffraction peaks below $2\theta=10°$ characteristic of two-dimensional materials. This provides strong evidence that the PFPAI only offers surface treatment of the perovskite and does not diffuse into the bulk of the film.

To further characterize the optical properties of passivated films, we measured the absorbance and PL of the films prepared on glass substrates. The normalized absorbance spectra of the films are shown in **Figure 2c**. The band gap of the films was derived from Tauc plots and PL peaks, the band gap of 1.64 eV was obtained for the standard film. Surprisingly, PFPAI treated films (50 mM, 100 mM, 200 mM, 500 mM, and 1000 mM) showed a band gap narrowing with enhanced absorption compared to the standard film. The band gap values are presented in **Table S1** (Supporting Information) and the Tauc plots are shown in the inset of **Figure 2c**. The PL spectra of the films were obtained at a pulse excitation wavelength of 630 nm and the normalized plots are shown in **Figure 2d**. As shown in **Figure 2d,** the emission wavelength for the standard film was observed at 760 nm whereas that of the 200 mM and 1000 mM PFPAI treated films were detected at 768 and 780 nm respectively. As previously mentioned, an increase in PFPAI concentration resulted in a gradual decrease in bromide ion concentration corresponding to increased substitution by iodide ions from PFPAI. It is thus expected that a decrease in the band gap of the resulting perovskite films would be observed with increased PFPAI concentration.

In order to validate the bromide ion to iodide ion substitution on treating the films with PFPAI, quantitative halide elemental analysis of the standard and PFPAI treated films (200 and 500 mM) were carried out using X-ray photoelectron spectroscopy as shown in **Figure S5a,b**. For this, the Br and I (3d) peaks in both cases were analyzed. In the case of the film, a prominent peak

corresponding to the Br (3d) core level was detected at a binding energy of 69.6 eV. Although the Br (3d) core level at the same binding energy (69.6eV) was also observed for the PFPAI treated films, the peak area observed was smaller than that of the standard film. Peak area analysis of Br (3d) revealed that the bromide ion concentration in the 500 mM PFPAI treated film is less than that present in the 200 mM PFPAI treated films which are in turn, lower than that in the standard as shown in **Figure S5a**. Similarly, for the standard film, two intense peaks corresponding to the I (3d) core level were detected at a binding energy of 631.3 eV and 620 eV. The films treated with 200 mM and 500 mM PFPAI also shows I (3d) core peaks at the same binding energies (631.3eV and 620eV). However, the peak areas obtained for 200 mM and 500 mM systems showed larger than that of the standard film (**Figure S5b)**. From this analysis, it is evident that the iodide ion concentration in the films increases with PFPAI concentration. The quantitative elemental composition (atomic percentage of main elements like Pb, I, and Br) of standard and PFPAI surface treated films were analyzed by using scanning electron microscopy-energy dispersive X-ray (SEM-EDX) spectroscopy. The **Table S2** shows the atomic percentage (I/Pb and Br/Pb) ratios in the film and it clearly proves the bromide to iodide substitution upon surface passivation with PFPAI.

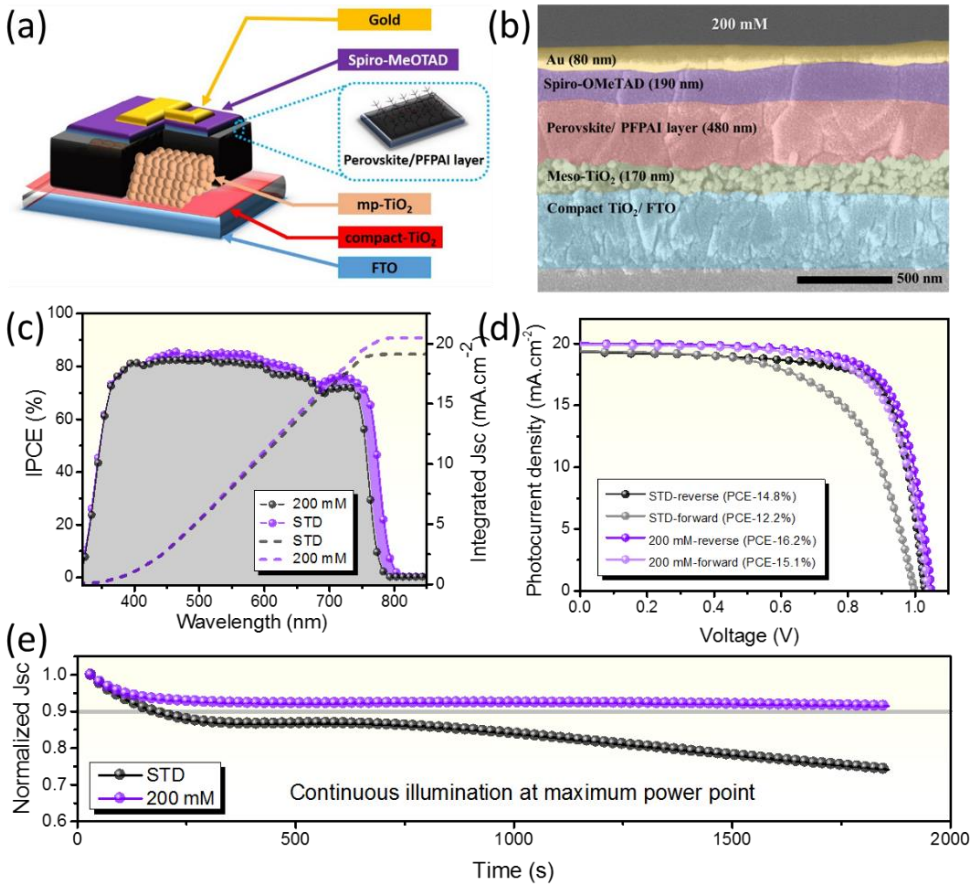

Figure 3. a) Perovskite solar cell architecture. b) Cross-sectional scanning electron microscopy (SEM) image of a perovskite solar cell device prepared with 200 mM PFPAI treated film. c) IPCE absorption spectra and integrated current density of standard and 200mM PFPAI treated film devices. d) Current-voltage (J-V) curves of standard and 200 mM PFPAI treated film device subjected to forward and reverse bias scan direction. e) Stabilized photocurrent density at maximum power point (PP_{max}) vs time for the unsealed standard and 200 mM PFPAI treated devices, the PP_{max} for standard and 200 mM PFPAI treated devices were found to be 0.83 and 0.85 V respectively.

To compare the performance of the standard and PFPAI treated films, solar cell devices were fabricated and tested. The device structure consists of Fluorine-doped tin oxide (FTO)/compact TiO_2 (c-TiO_2)/mesoporous TiO_2 (m-TiO_2)/Perovskite/Surface passivation layer/2,2',7,7'-tetrakis-(N,N-di-4-methoxyphenylamino)-9,9'-spirobifluorene (Spiro-MeOTAD)/Au as shown in **Figure 3a**. **Figure S8** shows the cross-sectional scanning electron microscopy (SEM) images of the solar cell devices prepared with standard triple-cation and 200 mM PFPAI treated perovskite films. The

relative thickness of the perovskite capping layer for both devices was found to be similar at approximately 490 nm.

The incident photon-to-current conversion efficiency (IPCE) spectra of the standard and 200 mM devices are shown in **Figure 3c**. The 200 mM PFPAI treated devices exhibited higher EQE than the standard over the wavelength range analogous to its absorbance regime, explaining the improved Jsc noted for the 200 mM PFPAI treated device. The integrated Jsc from EQE is in good agreement with the measured Jsc under simulated AM 1.5 G illumination. **Figure S9**, shows the IPCE comparison spectra of standard, 200 mM, 500 mM, and 1000 mM PFPAI treated devices over the wavelength range and it clearly manifests the spectral shift of a change in the IPCE absorption spectra. The 30 nm red-shifted IPCE absorption onset from 790 nm to 820 nm for the 1000 mM modified device with respect to the standard device also supports the hypothesis of band gap narrowing due to the substitution of bromide ions with iodide ions upon treating the surface with PFPAI.

Table 1. Photovoltaic performance parameters of perovskite solar cells of the standard and different concentrations of PFPAI. Average photovoltaic performance parameters of perovskite solar cells including the standard deviations of the short-circuit current density (*J*sc), open-circuit voltage (*V*oc), and fill factor (FF). The champion cell efficiencies for each PFPAI concentrations are given in brackets. The average statistical analysis is based on 10 solar cells on different substrates for each concentration of PFPAI.

Sample	Voc (V)	Jsc (mA cm^{-2})	FF (%)	PCE (%)
Standard	1.02 ± 0.009 (**1.03**)	19.1 ± 0.23 (**19.3**)	73.6 ± 1.2 (**74.2**)	14.6 ± 0.2 (**14.8**)
50 mM	1.05 ± 0.008 (**1.06**)	19.4 ± 0.12 (**19.6**)	73.2 ±1.02 (**73.6**)	15.2 ± 0.2 (**15.2**)
100 mM	1.06 ± 0.005 (**1.06**)	19.5 ± 0.15 (**19.6**)	75.3 ± 1.1 (**75.7**)	15.5 ± 0.1 (**15.5**)
200 mM	1.08 ± 0.011 (**1.08**)	19.8 ± 0.19 (**19.8**)	78.0 ± 1.0 (**78.4**)	16.4 ± 0.2 (**16.6**)

500 mM	0.98 ± 0.005 (**1.00**)	19.0 ± 0.22 (**19.1**)	71.0 ± 1.8 (**71.2**)	13.4 ± 0.3 (**13.4**)
1000 mM	0.85 ± 0.009 (**0.86**)	18.3 ± 0.38 (**18.7**)	63.1 ± 2.1 (**63.9**)	9.9 ± 0.2 (**10.1**)

The current density-voltage (*J–V*) curves of champion cells under a simulated air mass (AM) of 1 Sun illumination (100 mW cm^{-2}) is shown in **Figure 3d**. The device fabricated with standard triple-cation perovskite yielded an average PCE of 14.8% with an open circuit voltage (Voc), short-circuit current density (Jsc) and a fill factor (FF) of 1.03 V, 19.2 mA cm^{-2}, and 74% respectively. The optimum PFPAI concentration for the best device performance was found to be 200 mM, with all photovoltaic parameters of the devices listed in **Table 1**. The device fabricated with 200 mM modification gave an average PCE of 16.4% with an open circuit voltage (Voc) of 1.08 V, a short-circuit current density (Jsc) of 19.8 mA cm^{-2}, and a fill factor (FF) of 78% with better reproducibility compared to that of the standard. The improvement in performance of 200 mM PFPAI treated devices are due to the notable increase of Voc and Jsc and a slight increase in FF due to the presence of an optimal amount of PFPAI. The performance of 50 mM and 100 mM devices were comparatively better than that obtained for the standard; showing a PCE of 15.2% and 15.5% respectively. As the amount of PFPAI increased beyond 200mM, the performances of devices (500 mM and 1000 mM) gradually decreased, corresponding to reductions in Voc, Jsc, and FF with the devices were showed a PCE of 13.4% and 10.1% respectively. The reduced Voc and Jsc in 500 mM and 1000 mM can be attributed to the presence of more insulating hydrophobic passivation layer over the perovskite capping layer which resulted in detrimental effects on charge transport and recombination and as well as the dramatic changes in surface morphology by means of smaller grain sizes along with pinholes which altogether lower the device performance. **Figure**

3e, shows the comparison of stability performances of the standard and 200 mM PFPAI treated devices during a short-term test of 1850 sec; which shows that the passivation layer plays the vital role in the device stability.

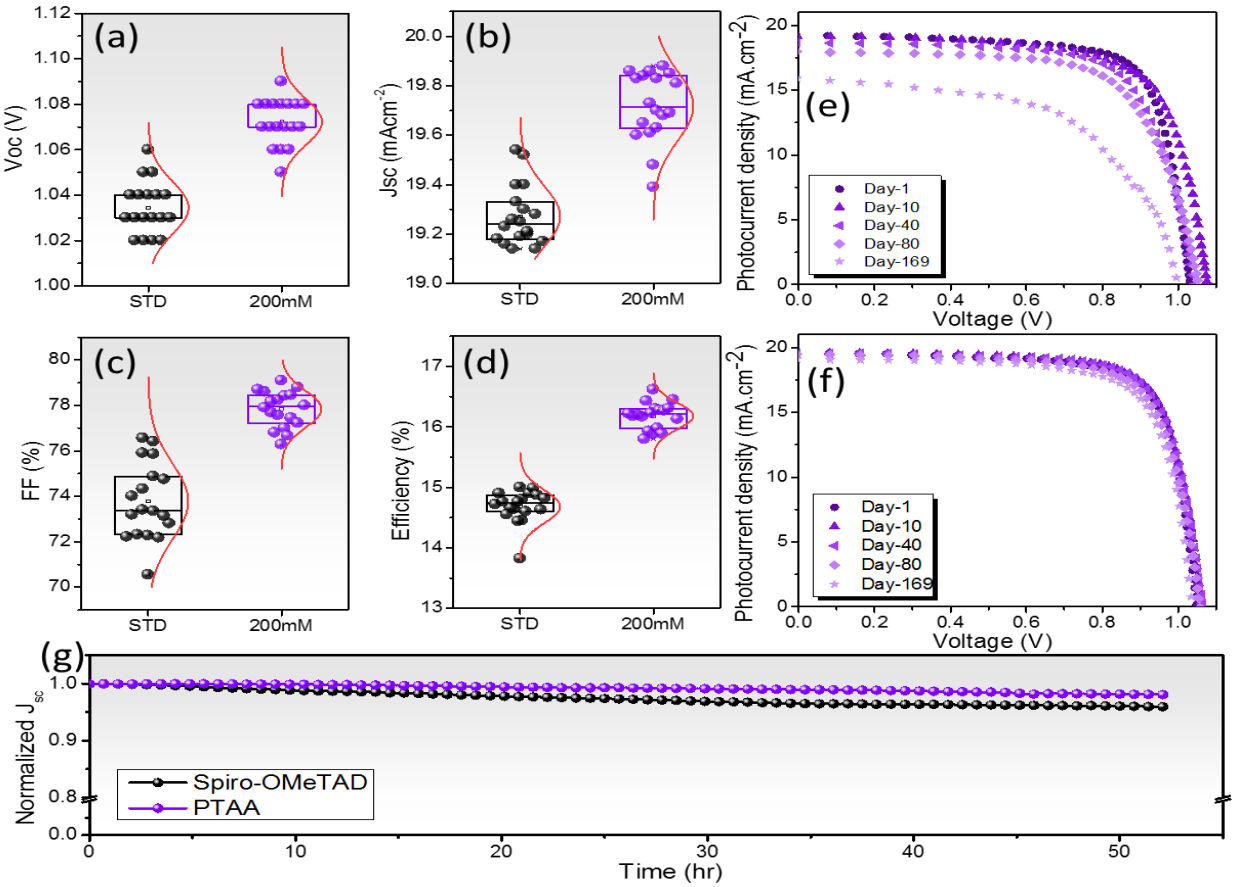

Figure 4. Statistical representation of 18 devices for standard and 200mM PFPAI treated for device parameters; a) Voc, b) Jsc, c) FF, and d) PCE. Aging test of the device based on e) standard, and f) 200 mM PFPAI treated devices. g) Stabilized photocurrent density at maximum power point (PP_{max}) vs time comparison for the 200 mM passivated unsealed devices with Spiro-MeOTAD and PTAA as hole-transport material under the N_2 atmosphere, the maximum power point value was at 0.80 V and 0.79 V for Spiro-MeOTAD and PTAA devices respectively.

The statistical analysis of device performance parameters of 18 devices for standard and 200 mM PFPAI treated are presented in **Figure 4a-d**. Hysteresis is the major bottleneck phenomenon commonly found in the J-V curves of perovskite solar cells and which originates majorly from ion migration or the presence of surface trap states.[42] As shown in **Figure 3d**, a device fabricated with 200 mM PFPAI treated films exhibited a Voc of 1.08 V, Jsc of 19.8 mA cm^{-2}, FF of 78%, and PCE

of 16.2% observed at reverse scan direction and Voc of 1.07 V, Jsc of 19.6 mA cm^{-2}, FF of 75%, and PCE of 15.1% at forward scan direction whereas the standard device exhibited a Voc of 1.03 V, Jsc of 19.2 mA cm^{-2}, FF of 75%, and PCE of 14.8% at reverse scan direction and Voc of 1.01 V, Jsc of 19.0 mA cm^{-2}, FF of 73%, and PCE of 12.2% at forward scan direction under 1 sun illumination. The reverse scan shows enhanced Voc, Jsc, FF, and PCE when compared to forward scan for 200 mM and standard devices. A negligible amount of hysteresis was observed in the case of 200 mM PFPAI treated device compared to the standard device and hysteresis index reduced from 0.17 (standard) to 0.06 (200 mM). The mitigation of hysteresis in the 200 mM PFPAI treated device can be favored by the reduction in surface trap defects and better interface modifications compared to the standard device.

To understand the effect of PFPAI passivation on perovskite capping layer towards the moisture, we have carried out stability studies of complete devices based on 200 mM and the standard under ambient environments (average RH =55% and 25 °C, at dark condition) without any encapsulation. The devices were monitored over a period 169 days and measured on the 10^{th}, 40^{th}, 80^{th} and 169^{th} day. During this period, the PCE of standard device dropped by about 40% from its initial value (14.8% to 9.0%), whereas the 200 mM PFPAI treated device retained ≈94% of its initial value (16.1% to 14.9%). From the stability data obtained, it can be concluded that by treating the perovskite surface with PFPAI, ingress of moisture into the capping layer can be significantly suppressed. A difference in the performance was also noted when the samples were tested under an extremely humid condition (~90% RH). The J-V comparison plot of standard and 200 mM PFPAI treated devices over 169 days is shown in **Figure 4e, f**. The overall aging data for the various device parameters such as Voc, Jsc, FF, and PCE are shown in **Figure S10** (Supporting Information). **Figure 4g** shows the stabilized photocurrent density in terms of maximum power

point against time to compare the performance of unsealed 200 mM PFPAI treated devices prepared with Spiro-MeOTAD and PTAA as hole-transport material under N_2 atmosphere. It was found that the devices employing PTAA as the hole-transporting material showcased better stability towards long-term light soaking of more than 55 hours when compared to the state-of-the-art Spiro-MeOTAD devices.

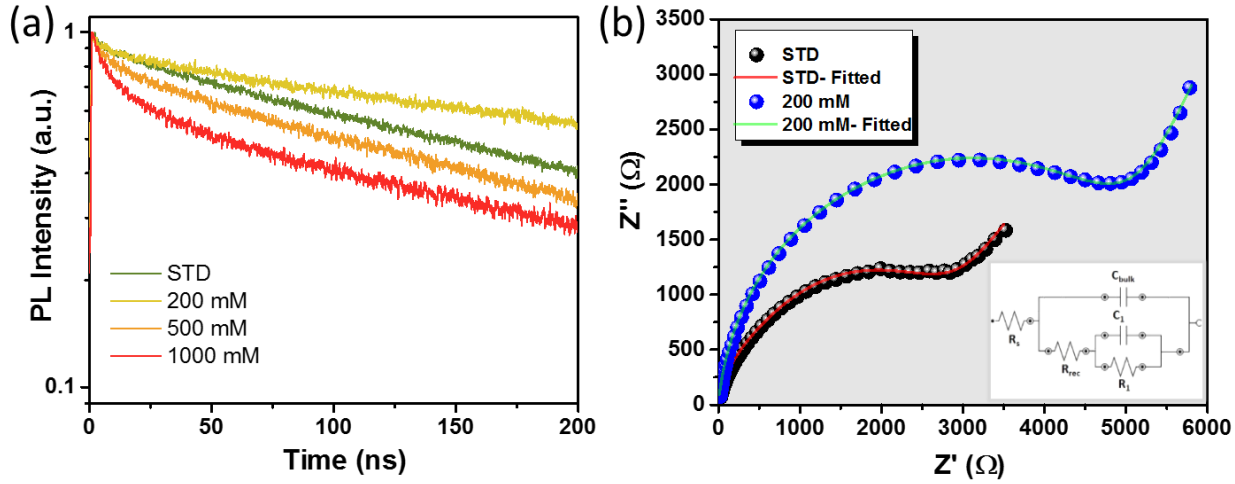

Figure 5. a) Time-resolved Photoluminescence (TRPL) spectra of standard and PFPAI treated films prepared on glass substrates. b) Nyquist plot of the standard and 200 mM modified devices under dark at 0.4 V bias, (Inset: Equivalent circuit model used for fitting the plots of standard and 200 mM PFPAI treated device (R_s, series resistance; R_1, bulk recombination resistance; R_{rec}, surface recombination resistance; C_{bulk}, capacitance at the bulk; C_1, capacitance at the surface)).

The charge recombination dynamics in the standard and surface passivated (200 mM, 500mM, and 1000 mM) films were probed through time-resolved photoluminescence (TRPL) measurements (**Figure 5a)**. All the PL curves were fitted with a double exponential decay function **Equation S1** (Supporting Information), to deconvolute the fast and slower decay kinetics. By analyzing the data in **Figure 5a** and **Table S3** (Supporting Information), the 200 mM PFPAI treated perovskite film exhibited longer lifetime for both slow and fast recombination processes compared to the standard film.

In order to gain more insight into the interfacial charge transport dynamics in the devices,[43-45] electrochemical impedance spectroscopy (EIS) measurements were carried out for the standard

and the 200mM PFPAI treated devices under dark in the ambient conditions. The device impedance was measured by applying 10 mV AC voltage whose frequency is swept from 100 Hz to 1 MHz in 100 equal steps on a logarithmic scale. The Nyquist plots of these devices were recorded at different applied voltages (0.2, 0.4, 0.5, 0.6, 0.8, 0.9, and 1 V) as shown in **Figure S11a,b**. The impedance spectra exhibited two arcs in the complex impedance plot as reported[46-47] elsewhere for devices with good charge extraction. As shown in **Figure 5b** (Supporting Information), the Nyquist plot of standard and 200 mM PFPAI treated devices at an applied voltage of 0.4 V and the data was analyzed using the commonly reported equivalent circuit[46-47] consisting of a series resistance (R_s), two capacitive (C_{bulk} and C_1) and two resistive components (R_{rec} and R_1). The series resistance arises from the ohmic contribution from wires and contacts. The low-frequency arc is contributed by R_1 and C_1 and is generally related to surface charge accumulation at the interfaces, ionic motion, etc.[48] C_{bulk} and R_{rec} define the high-frequency arc (10^5 Hz - 200 Hz), where C_{bulk} is related to the dielectric properties of the perovskite layer. Even though the exact origin of the associated resistances R_{rec} and R_1 are unknown, both are generally linked to surface as well as bulk charge recombination mechanisms in the device. It can be seen that for 200mM PFPAI treated devices, the arc at high-frequency regime (10^5 Hz - 200 Hz) is larger when compared to the standard device suggesting a higher recombination resistance (R_{rec}) for the PFPAI treated sample. This manifests well with the increased Voc, Jsc, and carrier lifetime of the 200 mM PFPAI treated sample suggesting trap passivation at the surface resulting in reduced recombination. This, in combination with an improved optical absorption window results in higher power conversion efficiencies.

In conclusion, we have successfully demonstrated bandgap narrowing by halide substitution in well-defined triple-cation perovskite structure through surface passivation using PFPAI. The

bromide ions in triple-cation perovskite assists in the formation of stable and high-quality perovskite thin films and further it has been substituted by iodide ions which were identified from the surface analysis. The widening in absorption window depends on the concentrations of surface passivator PFPAI which have been monitored through optical absorption of perovskite films and IPCE of the devices. At an optimized amount of PFPAI (200 mM), perovskite solar cells exhibited an enhanced PCE from 14.8% (standard) to 16.6%, which is attributed to the improvement in short-circuit current density (Jsc), open circuit voltage (Voc), and fill factor (FF). The PFPAI modified devices exhibited superior moisture stability compared to the standard under a relative humidity (RH) of 55 % and these perovskite solar cells displayed remarkable stability for 169 days under an ambient atmosphere without any encapsulation, retaining above 95% of its initial PCE. In addition, PFPAI could effectively passivate the perovskite surface and grain boundaries which resulted in reduced charge carrier recombination, increased charge carrier lifetime and thereby an enhanced device performance. Our findings may pave a new method for further optimization of highly efficient triple-cations perovskite with respect to its morphology, electronic properties, and stability towards efficient and reliable PV technology.

ASSOCIATED CONTENT

Supporting Information

Experimental details, characterization method, and additional data

AUTHOR INFORMATION

Corresponding Author

*Email: Nripan@ntu.edu.sg

Notes

The authors declare no competing financial interest.

ACKNOWLEDGMENT

This research was supported by the National Research Foundation, Prime Minister's Office, Singapore under its Competitive Research Programme (CRP Award No. NRF-CRP14-2014-03) and through the Singapore–Berkeley Research Initiative for Sustainable Energy (SinBeRISE) CREATE Program. The authors acknowledge Dr. Chen Shi for conducting XPS measurements.

REFERENCES

(1) Gratzel, M. The Light and Shade of Perovskite Solar Cells. *Nat. Mater.* **2014**, *13* (9), 838-842.

(2) Han, G.; Zhang, S.; Boix, P. P.; Wong, L. H.; Sun, L.; Lien, S.-Y. Towards High Efficiency Thin Film Solar Cells. *Prog. Mater Sci.* **2017**, 87, 246-291.

(3) Hao, F.; Stoumpos, C. C.; Cao, D. H.; Chang, R. P. H.; Kanatzidis, M. G. Lead-Free Solid-State Organic-Inorganic Halide Perovskite Solar Cells. *Nat. Photonics* **2014**, *8* (6), 489-494.

(4) Yang, W. S.; Noh, J. H.; Jeon, N. J.; Kim, Y. C.; Ryu, S.; Seo, J.; Seok, S. I. High-Performance Photovoltaic Perovskite Layers Fabricated Through Intramolecular Exchange. *Science* **2015**, *348* (6240), 1234-1237.

(5) Seo, J.; Noh, J. H.; Seok, S. I. Rational Strategies for Efficient Perovskite Solar Cells. *Acc. Chem. Res.* **2016**, *49* (3), 562-572.

(6) McMeekin, D. P.; Sadoughi, G.; Rehman, W.; Eperon, G. E.; Saliba, M.; Hörantner, M. T.; Haghighirad, A.; Sakai, N.; Korte, L.; Rech, B.; et al. A Mixed-Cation Lead Mixed-Halide Perovskite Absorber for Tandem Solar Cells. *Science* **2016**, *351* (6269), 151-155.

(7) Eperon, G. E.; Stranks, S. D.; Menelaou, C.; Johnston, M. B.; Herz, L. M.; Snaith, H. J. Formamidinium Lead Trihalide: A Broadly Tunable Perovskite for Efficient Planar Heterojunction Solar Cells. *Energy Environ. Sci.* **2014**, *7* (3), 982-988.

(8) Ogomi, Y.; Morita, A.; Tsukamoto, S.; Saitho, T.; Fujikawa, N.; Shen, Q.; Toyoda, T.; Yoshino, K.; Pandey, S. S.; Ma, T.; et al. $CH_3NH_3Sn_xPb_{(1-x)}I_3$ Perovskite Solar Cells Covering up to 1060 nm. *J. Phys. Chem. Lett.* **2014**, *5* (6), 1004-1011.

(9) Noh, J. H.; Im, S. H.; Heo, J. H.; Mandal, T. N.; Seok, S. I. Chemical Management for Colorful, Efficient, and Stable Inorganic–Organic Hybrid Nanostructured Solar Cells. *Nano Lett.* **2013**, *13* (4), 1764-1769.

(10) Lin, Q.; Armin, A.; Nagiri, R. C. R.; Burn, P. L.; Meredith, P. Electro-Optics of Perovskite Solar Cells. *Nat. Photonics* **2015**, *9* (2), 106-112.

(11) Shi, D.; Adinolfi, V.; Comin, R.; Yuan, M.; Alarousu, E.; Buin, A.; Chen, Y.; Hoogland, S.; Rothenberger, A.; Katsiev, K.; et al. Low Trap-State Density and Long Carrier Diffusion in Organolead Trihalide Perovskite Single Crystals. *Science* **2015**, *347* (6221), 519-522.

(12) Dong, Q.; Fang, Y.; Shao, Y.; Mulligan, P.; Qiu, J.; Cao, L.; Huang, J. Electron-Hole Diffusion Length > 175 μm in Solution-Grown $CH_3NH_3PbI_3$ Single Crystals. *Science* **2015**, *347* (6225), 967-970.

(13) Saidaminov, M. I.; Abdelhady, A. L.; Murali, B.; Alarousu, E.; Burlakov, V. M.; Peng, W.; Dursun, I.; Wang, L.; He, Y.; Maculan, G.; et al. High-Quality Bulk Hybrid Perovskite Single Crystals Within Minutes by Inverse Temperature Crystallization. *Nat. Commun.* **2015**, *6*, 7586.

(14) Stranks, S. D.; Eperon, G. E.; Grancini, G.; Menelaou, C.; Alcocer, M. J. P.; Leijtens, T.; Herz, L. M.; Petrozza, A.; Snaith, H. J. Electron-Hole Diffusion Lengths Exceeding 1 Micrometer in an Organometal Trihalide Perovskite Absorber. *Science* **2013**, *342* (6156), 341-344.

(15) Xing, G.; Mathews, N.; Sun, S.; Lim, S. S.; Lam, Y. M.; Grätzel, M.; Mhaisalkar, S.; Sum, T. C. Long-Range Balanced Electron- and Hole-Transport Lengths in Organic-Inorganic $CH_3NH_3PbI_3$. *Science* **2013**, *342* (6156), 344-347.

(16) Han, Q.; Bae, S.-H.; Sun, P.; Hsieh, Y.-T.; Yang, Y.; Rim, Y. S.; Zhao, H.; Chen, Q.; Shi, W.; Li, G.; et al. Single Crystal Formamidinium Lead Iodide ($FAPbI_3$): Insight into the Structural, Optical, and Electrical Properties. *Adv. Mater.* **2016**, *28* (11), 2253-2258.

(17) Kojima, A.; Teshima, K.; Shirai, Y.; Miyasaka, T. Organometal Halide Perovskites as Visible-Light Sensitizers for Photovoltaic Cells. *J. Am. Chem. Soc.* **2009**, *131* (17), 6050-6051.

(18) Li, X.; Bi, D.; Yi, C.; Décoppet, J.-D.; Luo, J.; Zakeeruddin, S. M.; Hagfeldt, A.; Grätzel, M. A Vacuum Flash–Assisted Solution Process for High-Efficiency Large-Area Perovskite Solar Cells. *Science* **2016**, 353 (6294), 58-62.

(19) National Renewable Energy Laboratory, Best Research-Cell Efficiencies Chart. https://www.nrel.gov/pv/assets/images/efficiency-chart.png (accessed January 2018).

(20) Xing, G.; Mathews, N.; Lim, S. S.; Yantara, N.; Liu, X.; Sabba, D.; Grätzel, M.; Mhaisalkar, S.; Sum, T. C. Low-Temperature Solution-Processed Wavelength-Tunable Perovskites for Lasing. *Nat. Mater.* **2014**, *13* (5), 476-480.

(21) Zhu, H.; Fu, Y.; Meng, F.; Wu, X.; Gong, Z.; Ding, Q.; Gustafsson, M. V.; Trinh, M. T.; Jin, S.; Zhu, X. Y. Lead Halide Perovskite Nanowire Lasers with Low Lasing Thresholds and High Quality Factors. *Nat. Mater.* **2015**, *14* (6), 636-642.

(22) Saliba, M.; Wood, S. M.; Patel, J. B.; Nayak, P. K.; Huang, J.; Alexander-Webber, J. A.; Wenger, B.; Stranks, S. D.; Hörantner, M. T.; Wang, J. T.-W.; et al. Structured Organic–Inorganic Perovskite Toward a Distributed Feedback Laser. *Adv. Mater.* **2016**, *28* (5), 923-929.

(23) Ling, Y.; Yuan, Z.; Tian, Y.; Wang, X.; Wang, J. C.; Xin, Y.; Hanson, K.; Ma, B.; Gao, H. Bright Light-Emitting Diodes Based on Organometal Halide Perovskite Nanoplatelets. *Adv. Mater.* **2016**, *28* (2), 305-311.

(24) Yantara, N.; Bhaumik, S.; Yan, F.; Sabba, D.; Dewi, H. A.; Mathews, N.; Boix, P. P.; Demir, H. V.; Mhaisalkar, S. Inorganic Halide Perovskites for Efficient Light-Emitting Diodes. *J. Phys. Chem. Lett.* **2015**, *6* (21), 4360-4364.

(25) Veldhuis, S. A.; Boix, P. P.; Yantara, N.; Li, M.; Sum, T. C.; Mathews, N.; Mhaisalkar, S. G. Perovskite Materials for Light-Emitting Diodes and Lasers. *Adv. Mater.* **2016**, *28* (32), 6804-6834.

(26) Domanski, K.; Tress, W.; Moehl, T.; Saliba, M.; Nazeeruddin, M. K.; Grätzel, M. Working Principles of Perovskite Photodetectors: Analyzing the Interplay Between Photoconductivity and Voltage-Driven Energy-Level Alignment. *Adv. Funct. Mater.* **2015**, *25* (44), 6936-6947.

(27) Su, L.; Zhao, Z. X.; Li, H. Y.; Yuan, J.; Wang, Z. L.; Cao, G. Z.; Zhu, G. High-Performance Organolead Halide Perovskite-Based Self-Powered Triboelectric Photodetector. *ACS Nano* **2015**, *9* (11), 11310-11316.

(28) Wei, H.; Fang, Y.; Mulligan, P.; Chuirazzi, W.; Fang, H.-H.; Wang, C.; Ecker, B. R.; Gao, Y.; Loi, M. A.; Cao, L.; et al. Sensitive X-ray Detectors Made of Methylammonium Lead Tribromide Perovskite Single Crystals. *Nat. Photonics* **2016**, *10* (5), 333-339.

(29) Chin, X. Y.; Cortecchia, D.; Yin, J.; Bruno, A.; Soci, C. Lead Iodide Perovskite Light-Emitting Field-Effect Transistor. *Nat. Commun.* **2015**, *6*, 7383.

(30) Lee, J.-W.; Seol, D.-J.; Cho, A.-N.; Park, N.-G. High-Efficiency Perovskite Solar Cells Based on the Black Polymorph of $HC(NH_2)_2PbI_s$. *Adv. Mater.* **2014**, *26* (29), 4991-4998.

(31) Saliba, M.; Matsui, T.; Seo, J.-Y.; Domanski, K.; Correa-Baena, J.-P.; Nazeeruddin, M. K.; Zakeeruddin, S. M.; Tress, W.; Abate, A.; Hagfeldt, A. Cesium-Containing Triple Cation Perovskite Solar Cells: Improved Stability, Reproducibility and High Efficiency. *Energy Environ. Sci.* **2016**, *9* (6), 1989-1997.

(32) Yang, M.; Zeng, Y.; Li, Z.; Kim, D. H.; Jiang, C.-S.; van de Lagemaat, J.; Zhu, K. Do Grain Boundaries Dominate Non-Radiative Recombination in $CH_3NH_3PbI_3$ Perovskite Thin Films?. *Phys. Chem. Chem. Phys.* **2017**, *19* (7), 5043-5050.

(33) Han, G.; Koh, T. M.; Lim, S. S.; Goh, T. W.; Guo, X.; Leow, S. W.; Begum, R.; Sum, T. C.; Mathews, N.; Mhaisalkar, S. Facile Method to Reduce Surface Defects and Trap Densities in Perovskite Photovoltaics. *ACS Appl. Mater. Interfaces* **2017**, 9 (25), 21292-21297.

(34) Zhou, H.; Chen, Q.; Li, G.; Luo, S.; Song, T.-b.; Duan, H.-S.; Hong, Z.; You, J.; Liu, Y.; Yang, Y. Interface Engineering of Highly Efficient Perovskite Solar Cells. *Science* **2014**, *345* (6196), 542-546.

(35) Edri, E.; Kirmayer, S.; Mukhopadhyay, S.; Gartsman, K.; Hodes, G.; Cahen, D. Elucidating the Charge Carrier Separation and Working Mechanism of $CH_3NH_3PbI_{3-x}Cl_x$ Perovskite Solar Cells. *Nat. Commun.* **2014**, *5*, 3461.

(36) Li, B.; Zheng, C.; Liu, H.; Zhu, J.; Zhang, H.; Gao, D.; Huang, W. Large Planar π-Conjugated Porphyrin for Interfacial Engineering in p-i-n Perovskite Solar Cells. *ACS Appl. Mater. Interfaces* **2016**, *8* (41), 27438-27443.

(37) Cao, J.; Yin, J.; Yuan, S.; Zhao, Y.; Li, J.; Zheng, N. Thiols as Interfacial Modifiers to Enhance the Performance and Stability of Perovskite Solar Cells. *Nanoscale* **2015**, *7* (21), 9443-9447.

(38) Lin, Y.; Shen, L.; Dai, J.; Deng, Y.; Wu, Y.; Bai, Y.; Zheng, X.; Wang, J.; Fang, Y.; Wei, H.; et al. π-Conjugated Lewis Base: Efficient Trap-Passivation and Charge-Extraction for Hybrid Perovskite Solar Cells. *Adv. Mater.* **2017**, *29* (7), 1604545.

(39) Roldan-Carmona, C.; Gratia, P.; Zimmermann, I.; Grancini, G.; Gao, P.; Graetzel, M.; Nazeeruddin, M. K. High Efficiency Methylammonium Lead Triiodide Perovskite Solar Cells: The Relevance of Non-Stoichiometric Precursors. *Energy Environ. Sci.* **2015**, *8* (12), 3550-3556.

(40) Bi, D.; Tress, W.; Dar, M. I.; Gao, P.; Luo, J.; Renevier, C.; Schenk, K.; Abate, A.; Giordano, F.; Correa Baena, J.-P.; et al. Efficient Luminescent Solar Cells based on Tailored Mixed-Cation Perovskites. *Sci. Adv.* **2016**, *2* (1), e1501170.

(41) Jacobsson, T. J.; Correa-Baena, J.-P.; Halvani Anaraki, E.; Philippe, B.; Stranks, S. D.; Bouduban, M. E. F.; Tress, W.; Schenk, K.; Teuscher, J.; Moser, J.-E.; et al. Unreacted PbI_2 as a Double-Edged Sword for Enhancing the Performance of Perovskite Solar Cells. *J. Am. Chem. Soc.* **2016**, *138* (32), 10331-10343.

(42) Correa-Baena, J.-P.; Anaya, M.; Lozano, G.; Tress, W.; Domanski, K.; Saliba, M.; Matsui, T.; Jacobsson, T. J.; Calvo, M. E.; Abate, A.; et al. Unbroken Perovskite: Interplay of Morphology, Electro-Optical Properties, and Ionic Movement. *Adv. Mater.* **2016**, *28* (25), 5031-5037.

(43) Fabregat-Santiago, F.; Garcia-Belmonte, G.; Mora-Sero, I.; Bisquert, J. Characterization of Nanostructured Hybrid and Organic Solar Cells by Impedance Spectroscopy. *Phys. Chem. Chem. Phys.* **2011**, *13* (20), 9083-9118.

(44) Bisquert, J. Theory of the Impedance of Electron Diffusion and Recombination in a Thin Layer. *J. Phys. Chem. B* **2002**, *106* (2), 325-333.

(45) Bisquert, J.; Mora-Sero, I.; Fabregat-Santiago, F. Diffusion–Recombination Impedance Model for Solar Cells with Disorder and Nonlinear Recombination. *ChemElectroChem* **2014**, *1* (1), 289-296.

(46) Correa-Baena, J.-P.; Turren-Cruz, S.-H.; Tress, W.; Hagfeldt, A.; Aranda, C.; Shooshtari, L.; Bisquert, J.; Guerrero, A. Changes from Bulk to Surface Recombination Mechanisms between Pristine and Cycled Perovskite Solar Cells. *ACS Energy Lett.* **2017**, *2* (3), 681-688.

(47) Zarazua, I.; Han, G.; Boix, P. P.; Mhaisalkar, S.; Fabregat-Santiago, F.; Mora-Seró, I.; Bisquert, J.; Garcia-Belmonte, G. Surface Recombination and Collection Efficiency in Perovskite Solar Cells from Impedance Analysis. *J. Phys. Chem. Lett.* **2016**, *7* (24), 5105-5113.

(48) Kim, H.-S.; Mora-Sero, I.; Gonzalez-Pedro, V.; Fabregat-Santiago, F.; Juarez-Perez, E. J.; Park, N.-G.; Bisquert, J. Mechanism of Carrier Accumulation in Perovskite Thin-Absorber Solar Cells. *Nat. Commun.* **2013**, *4*, 2242.

Supporting Information

Extended Absorption Window and Improved Stability of Cesium-Based Triple-Cation Perovskite Solar Cells Passivated with Perfluorinated Organics

K. M. Muhammed Salim,[†] Teck Ming Koh,[†] Damodaran Bahulayan,[†] P. C. Harikesh,[‡] Nur Fadilah Jamaludin,[‡] Benny Febriansyah,[†] Annalisa Bruno,[†Δ] Subodh Mhaisalkar,[†§] and Nripan Mathews[†§]*

[†]Energy Research Institute @ NTU (ERI@N), Research Techno Plaza, X-Frontier Block, Level 5, 50 Nanyang Drive, Singapore 637553

[‡]Interdisciplinary Graduate School, Nanyang Technological University, 50 Nanyang Avenue, Singapore 639798

[Δ]Division of Physics and Applied Physics, School of Physical and Mathematical Sciences, Nanyang Technological University, 21 Nanyang Link, Singapore 637371

[§]School of Materials Science and Engineering, Nanyang Technological University, 50 Nanyang Avenue, Singapore 639798

Corresponding Author

*Email: Nripan@ntu.edu.sg

Experimental Section

Materials and methods

2,2,3,3,3-pentafluoropropyl ammonium iodide (PFPAI): 0.9 mL of hydroiodic acid (57 wt% in water) (Sigma-Aldrich) was dropped slowly into a solution containing 1 g of 2,2,3,3,3-pentafluoropropyl ammonium iodide (TCI) in methanol which was previously cooled to 0 °C. The amine to hydroiodic acid ratio is kept at 1:1.01. The solution was further stirred for 8 h at room temperature. A concentrated pale yellow solution was obtained by rotavapor and re-dissolved with a minimum amount of ethanol and prior to re-precipitation in diethyl ether. The resulting white solid was then collected and dried under vacuum for 1 day at 50˚C. ^{1}H NMR (400 MHz, DMSO-d6) δ 8.76 (s, 3H), 4.03–3.95 (t, 2H) ppm; ^{13}C-NMR (100 MHz, DMSO-d6) δ 37.95, 37.73, 37.52 ppm; ^{19}F NMR (DMSO-d6) δ 83.83, 119.71 ppm; MS (EI, 70 eV) (m/z) 150.09 (M^{+}, 100%).

Device fabrication

The fluorine-doped tin oxide (FTO) coated glass was etched with Zn powder (Sigma-Aldrich) and 4 M hydrochloric acid (Sigma-Aldrich) and followed by sequential cleaning with decon soap solution, deionized water, ethanol, and acetone. A thin compact layer of TiO_2 was deposited on the cleaned FTO by spray pyrolysis using N_2 as the carrying gas at 450°C from a precursor solution consisting of 0.6 mL titanium diisopropoxide and 0.4 mL bis(acetylacetonate) dissolved in 9 mL anhydrous Isopropanol (1:9 v/v ratio). The TiO_2 compact layer was further treated with 50 mM of $TiCl_4$ solution at 70 °C for 30 minutes, followed by washing with deionized water and ethanol solution. The substrate was finally calcined at 500°C for 30 min. A mesoporous TiO_2 film was subsequently deposited by spin-coating TiO_2 paste (30 NR-D, Dyesol) diluted with absolute ethanol (1:5.5 w/w), the substrate was immediately dried on a hotplate at 100°C, and again calcined at 500°C for 30 min.

The triple cation perovskite, $(FA_{0.83}MA_{0.17})_{0.95}Cs_{0.05}Pb(I_{0.83}Br_{0.17})_3$ layer was deposited by single step method as reported earlier.[1] FAI and MABr are purchased from Dyesol. PbI_2 and $PbBr_2$ are from TCI, and CsI is from Sigma Aldrich. A mixed solution of FAI (1 M), PbI_2 (1.1 M), MABr (0.2 M) and $PbBr_2$ (0.2 M) was dissolved in dimethylformamide (DMF) and dimethyl sulfoxide (DMSO) (4:1, v/v) with an excess amount

of PbI_2. 1.5 M solution of CsI was added into the mixed solution forming the composition required. The triple cation solution was spin-coated on the substrate with a two steps program at 2000 rpm and 6000 rpm for 10 s and 30 s respectively. During the second step, 100 µL chlorobenzene was dropped on the spinning substrate after 20 s. The substrate was then annealed at 100 °C for 45 min. Different concentrations (50, 100, 200, 500, and 1000 mM) of PFPAI solution in 2- propanol was spin coated on top of annealed perovskite films at 4000 rpm for 30 s. The film was further annealed at 70 °C for 10 min. Subsequently, the Spiro-OMeTAD solution was deposited atop of the perovskite layer by spin coating at 4000 rpm for 30 s. Spiro-OMeTAD solutions was prepared by dissolving Spiro-OMeTAD (70 mg/mL in chlorobenzene) (Sigma Aldrich) and followed by the addition of tert-butyl pyridine (t-BP), Lithium bis(trifluoromethylsulfonyl) imide (LiTFSI) (Sigma Aldrich) in acetonitrile, and FK 102 (Tris(2-(1H-pyrazol-1-yl)-4-tert-butylpyridine)- cobalt(II) Tris(bis(trifluoromethylsulfonyl)imide)) in acetonitrile to the above solution. Finally, 90 nm of gold counter electrode was deposited using thermal evaporation method. For PTAA devices, the solution was prepared by dissolving PTAA (10 mg/ mL in toluene) (Sigma Aldrich) with additives in toluene. The additives like Li-TFSI (7.5 µL) from the stock solution (170 mg in 1 mL acetonitrile) and tert-butyl pyridine (t-BP) (4 µL) were added. PTAA solution was deposited atop of the perovskite layer by spin coating at 4000 rpm for 30 s. Finally, 90 nm of gold counter electrode was deposited using thermal evaporation method.

Characterization

XRD: The crystallographic information of the films were analyzed by Bruker AXS (D8 ADVANCE) X-Ray diffractometer with Cu Kα radiation and the step size of 0.04° and stepping time of 1 s. The X-Ray diffraction patterns were recorded from films deposited on top of the glass.

X-ray Photoelectron spectroscopy (XPS): XPS measurements were performed using Omicron EA-125 hemispherical electron analyzer under UHV conditions ($<1\times10^{-9}$ torr). An air-tight sample container was used to transfer the samples from glove box to the load-lock chamber. A monochromatic Al-Kα source with $h\nu$ = 1486.6 eV, 200 W was used for XPS measurements. CAE mode was used in both XPS measurements. The pass energy for XPS was 50 eV for wide scans and 20 eV for elemental scans. Elemental analysis was done by fitting Gaussian-Lorentzian profile over Shirley background in each elemental scan.

UV-Vis Spectra: The absorptions spectra were obtained using a UV−vis spectrometer (SHIMADZU UV-3600 UV−vis-NIR Spectrophotometer) with an integrating sphere (ISR-3100).

SEM: The topographical and cross-sectional images were recorded by Field Emission Scanning Electron Microscopy (FESEM, JEOL, JSM 7600F).

I-V Measurements: Photovoltaic characterization was carried out using an AM 1.5G solar simulator equipped with a 450 W xenon lamp (model 81172, Oriel). Its power output was adjusted to match AM 1.5G sunlight (100 mW/ cm^2) by using a reference Si photodiode. I−V curves were obtained by applying an external bias to the cell and measuring the generated photocurrent with a Keithley model 2612A digital source meter. The voltage scan was done at 100 mV/s from −0.1 to +0.7 V with 121 intermediate points. All devices were measured by masking the active area with a black tape mask of 0.16 cm^2 area.

Incident-photon-to current conversion efficiency (IPCE): Measured using a PVE300 (Bentham), with a dual xenon/quartz halogen light source, measured in DC mode, with no bias light.

Time Resolved Photoluminescence (TRPL): For TRPL decay, the micro-PL setup was based on a fiber-coupled microscope system, employed a VIS-NIR microscope objective (10x, numerical aperture= 0.65). The samples were excited by using a picosecond-pulse light-emitting diode at 405 nm (Picoquant P-C-405B) with a 5 MHz repetition rate. The beam spot size was approximately 10 mm. The time-resolved decays were collected by using an Acton monochromator (SpectraPro 2300) fiber coupled to the microscope and detected by using a Micro Photon Devices single-photon avalanche photodiode. The signal was then acquired by a time-correlated single-photon counting card. The temporal resolution was approximately 5 ps.

NMR: ^{1}H, ^{13}C and ^{19}F NMR spectra were obtained using a Bruker Avance III-400 (400MHz), and are reported in ppm using a solvent as an internal standard: DMSO-d6. Data reported as: s= singlet, t= triplet.

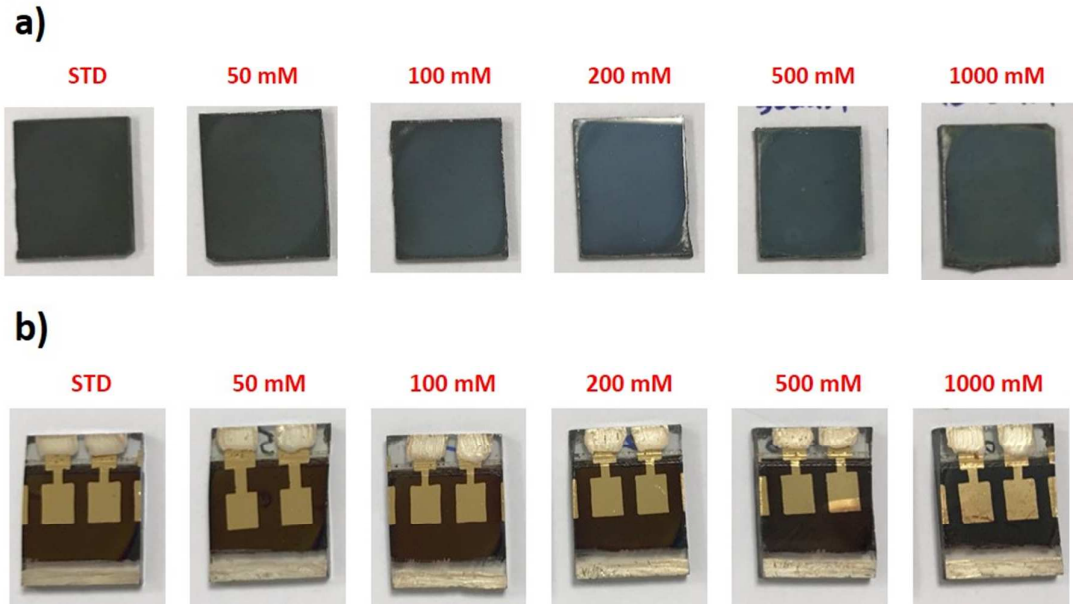

Figure S1. Photographic images of standard and PFPAI treated perovskite a) films and b) solar cell devices with a 0.4 cm x 0.4 cm active area.

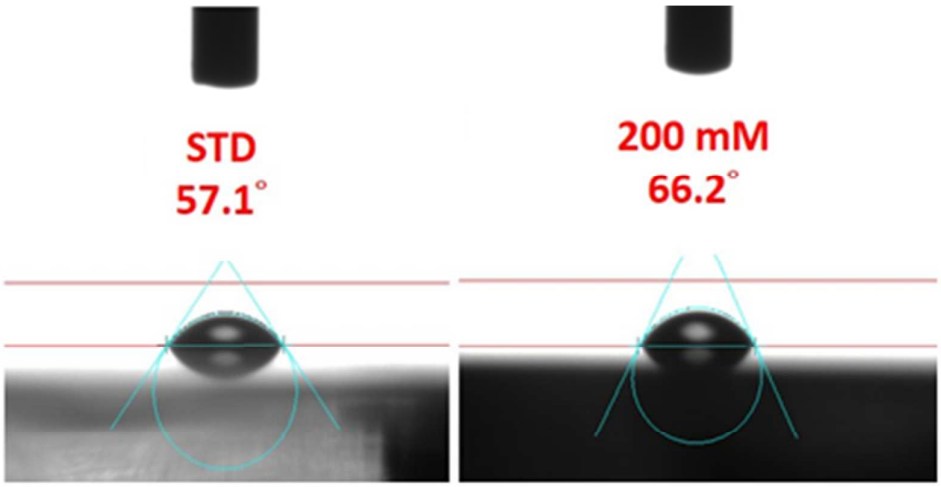

Figure S2. The static water contact angle of the standard film and 200 mM PFPAI treated film.

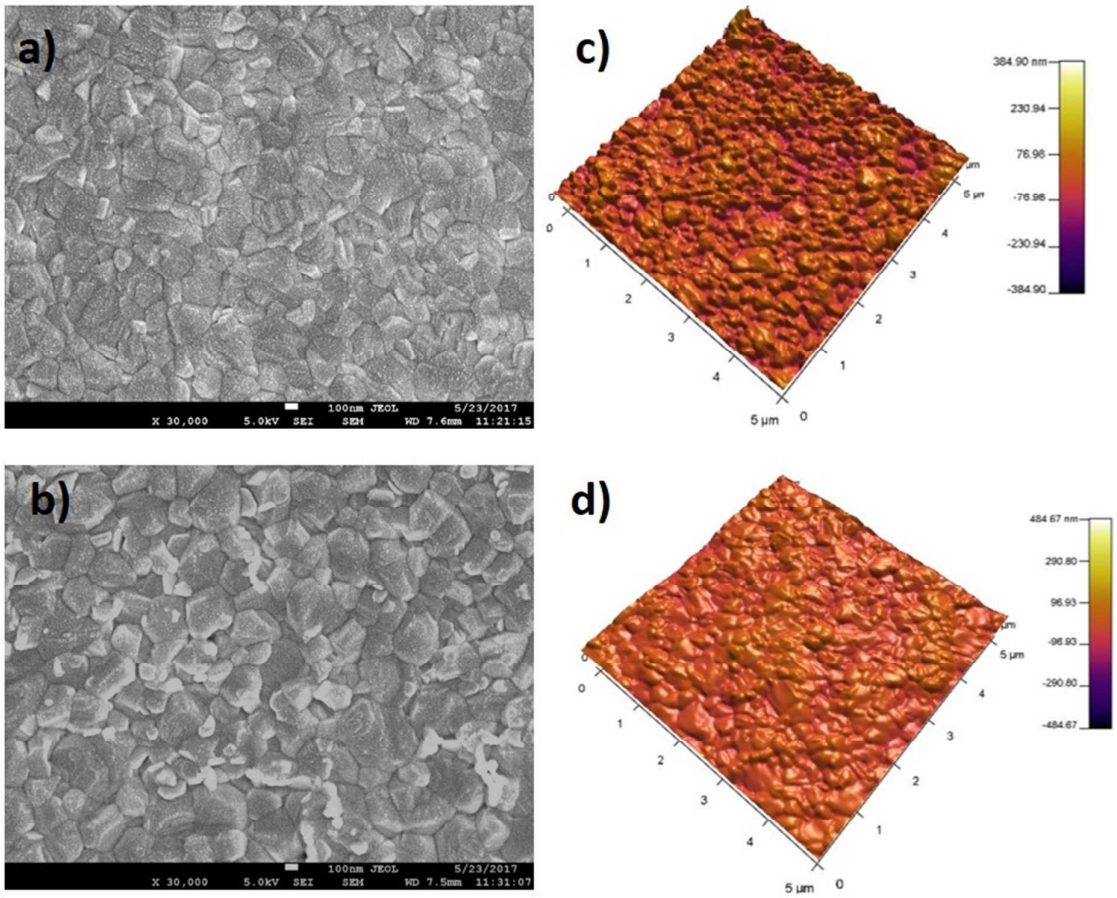

Figure S3. Morphologica**l** images of a) standard, and b) 200 mM PFPAI treated films on top of mesoporous TiO_2. Topological image of the surface of c) standard and d) 200 mM PFPAI treated films. The size of the AFM images is 5 x 5 μm^2.

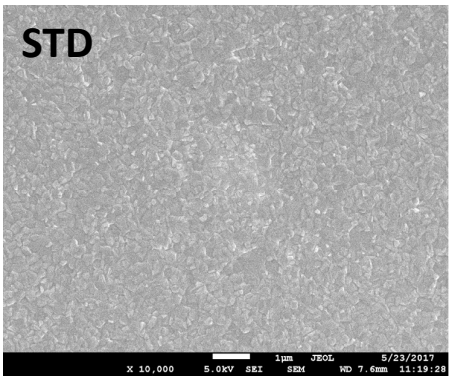
STD
1μm JEOL 5/23/2017
X 10,000 5.0kV SEI SEM WD 7.6mm 11:19:28

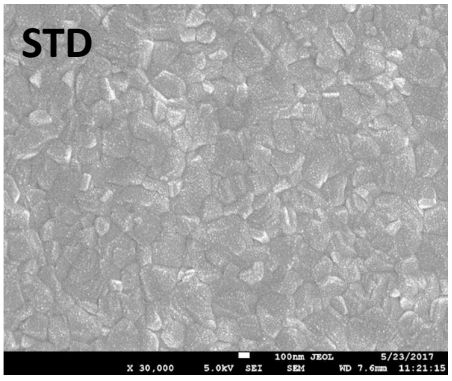
STD
100nm JEOL 5/23/2017
X 30,000 5.0kV SEI SEM WD 7.6mm 11:21:15

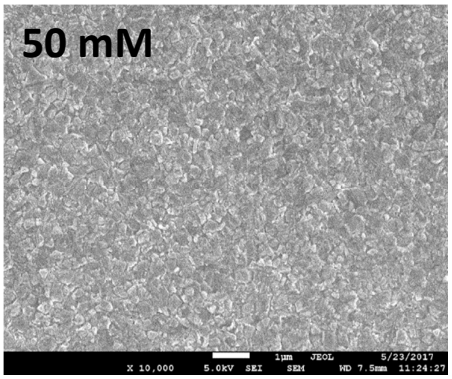
50 mM
1μm JEOL 5/23/2017
X 10,000 5.0kV SEI SEM WD 7.5mm 11:24:27

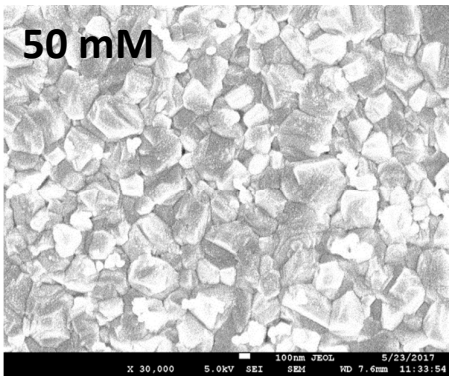
50 mM
100nm JEOL 5/23/2017
X 30,000 5.0kV SEI SEM WD 7.6mm 11:33:54

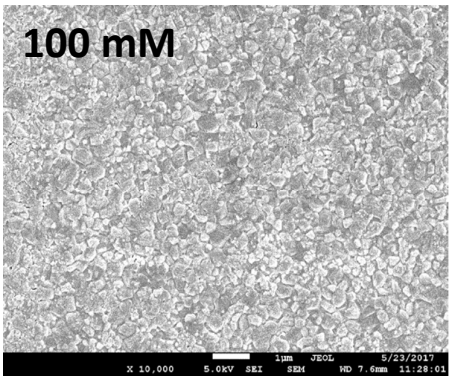
100 mM
1μm JEOL 5/23/2017
X 10,000 5.0kV SEI SEM WD 7.6mm 11:28:01

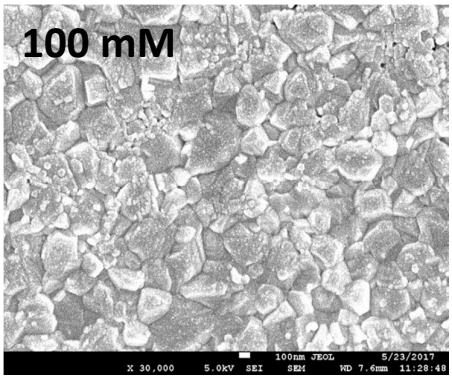
100 mM
100nm JEOL 5/23/2017
X 30,000 5.0kV SEI SEM WD 7.6mm 11:28:48

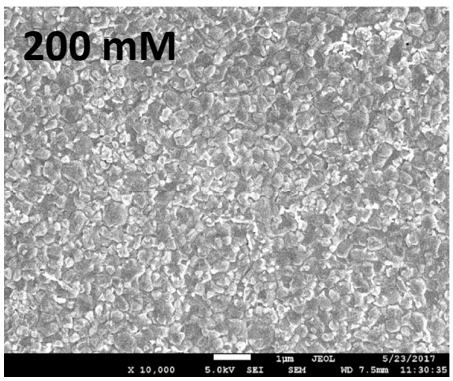
200 mM
1μm JEOL 5/23/2017
X 10,000 5.0kV SEI SEM WD 7.5mm 11:30:35

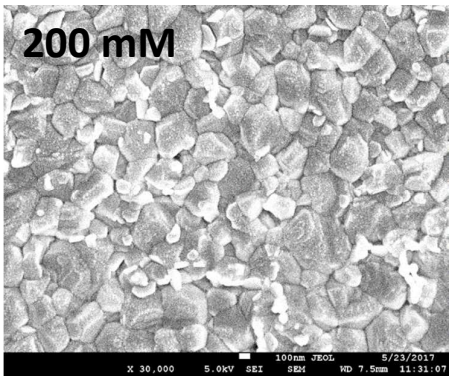
200 mM
100nm JEOL 5/23/2017
X 30,000 5.0kV SEI SEM WD 7.5mm 11:31:07

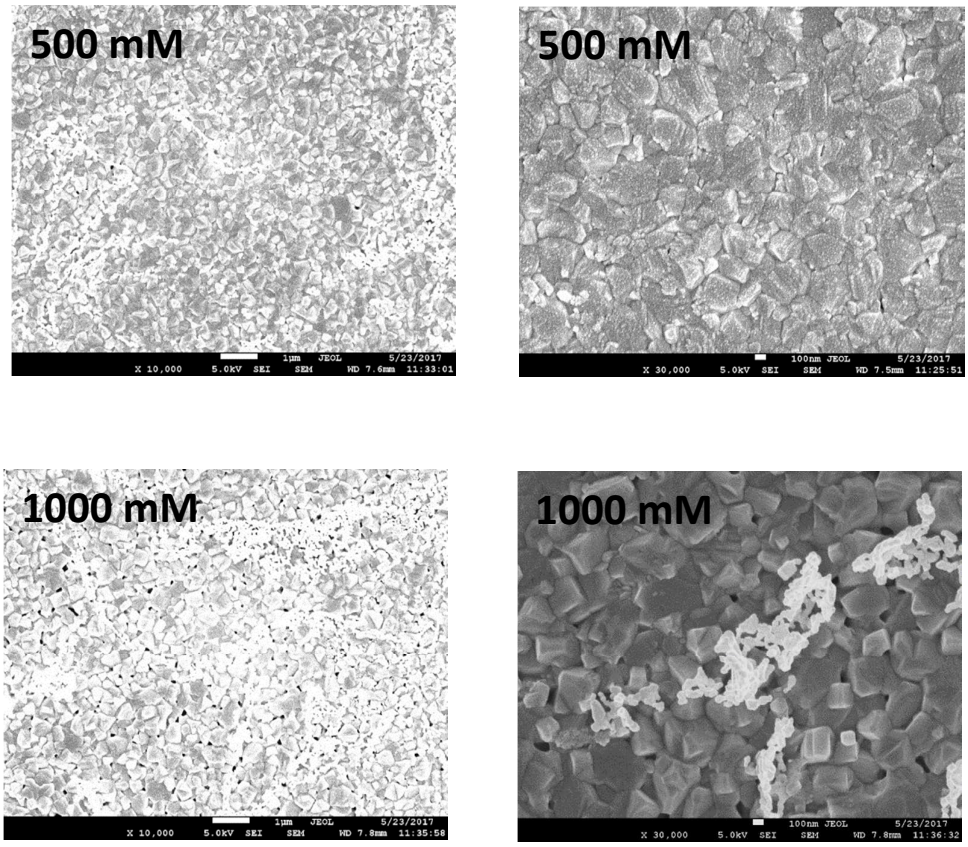

Figure S4. SEM images of standard and PFPAI treated perovskite films (50 mM, 100 mM, 200 mM, 500 mM, and 1000 mM). The scale bar for left and right images are 1 μm and 0.1 μm respectively.

Table S1. Shows the band gap value of perovskite films (STD, 50 mM, 100 mM, 200 mM, 500 mM and 1000 mM) calculated from the Tauc Plots.

Sample	Band gap (eV)
STD	1.640
50 mM	1.633
100 mM	1.623
200 mM	1.619
500 mM	1.610
1000 mM	1.602

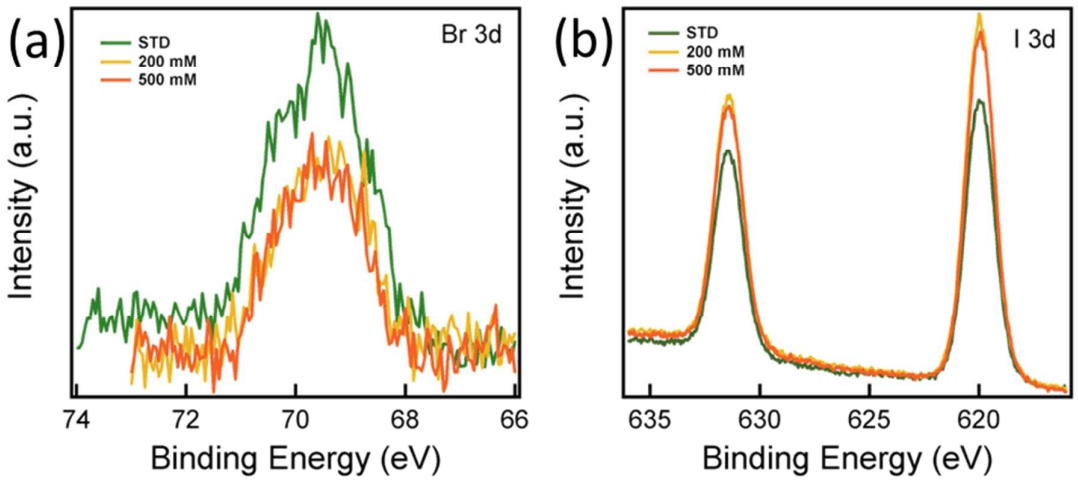

Figure S5. Quantitative surface elemental analysis of a) bromide (Br-3d) and b) iodide (I-3d) in standard and PFPAI treated films (200 mM, and 500 mM).

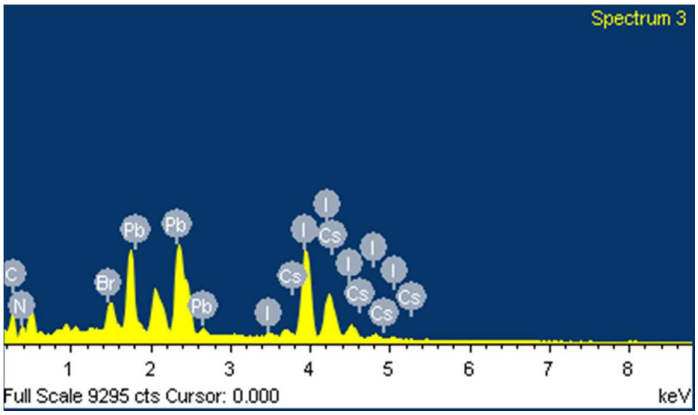

Figure S6. SEM-EDX elemental analysis spectra of standard triple cation film.

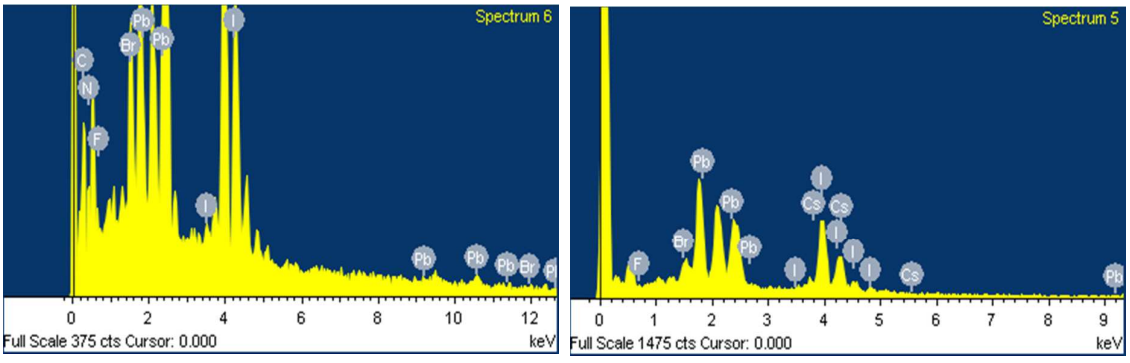

Figure S7. SEM-EDX elemental analysis spectra of 200 mM surface passivated film with PFPAI. Only the trace amounts of fluorine were detected from the sample due to the detection limit of EDX.

Table S2. Atomic percentage of main elements (Pb, I, and Br) in the STD, 100 mM, 200 mM, 500 mM and 1000 mM films measured using EDX

Sample	Atomic % of Pb	Atomic % of I	Atomic % of Br	I/Pb atomic ratio	Br/Pb atomic ratio
STD	24.75	57.53	17.72	2.32	0.71
100 mM	23.54	61.21	15.25	2.60	0.64
200 mM	23.33	63.47	13.20	2.72	0.56
500 mM	23.57	67.54	8.89	2.86	0.37
1000 mM	20.43	75.08	4.49	3.67	0.21

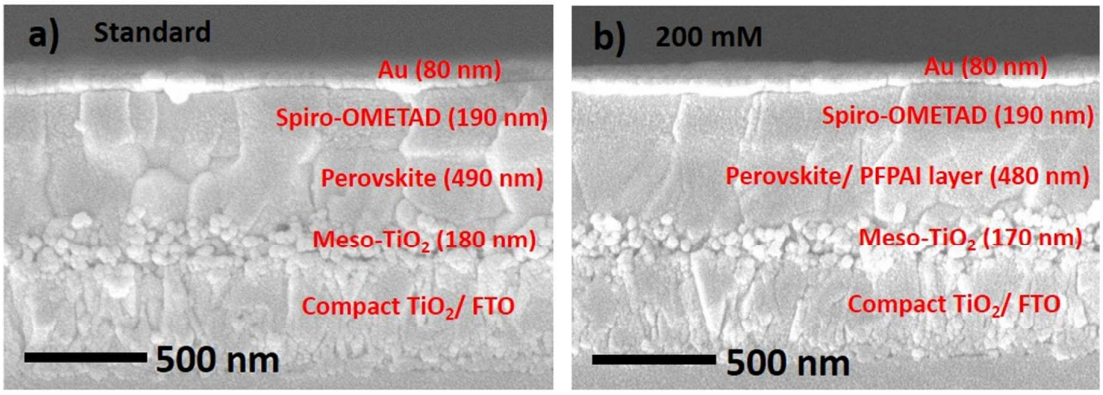

Figure S8. Cross-sectional scanning electron microscopy (SEM) images of a perovskite solar cell device prepared with a) standard triple cation and b) 200 mM PFPAI treatment. The device architecture consists of F-doped tin oxide (FTO)/ compact TiO_2 (c-TiO_2)/ mesoporous TiO_2 (m-TiO_2)/ Perovskite/Surface passivation layer (PFPAI layer)/ 2,2',7,7'-tetrakis-(N,N-di-4-methoxyphenylamino)-9,9'-spirobifluorene (Spiro-MeOTAD)/Au.

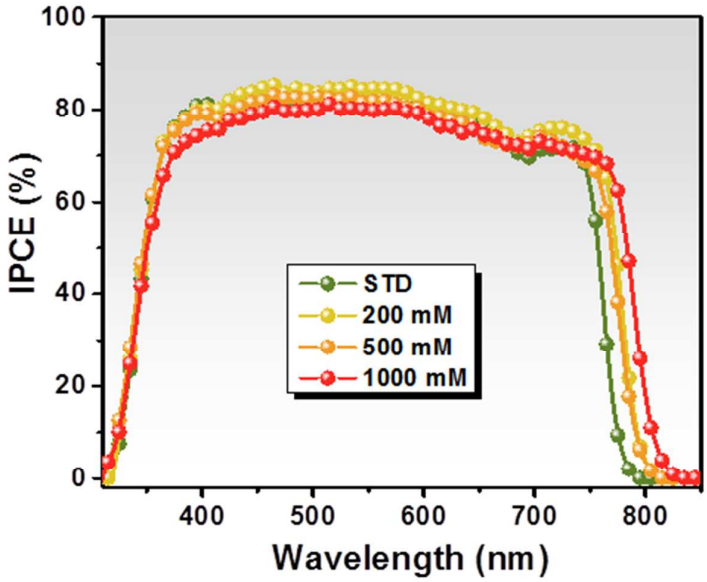

Figure S9. IPCE (incident photon-to-current conversion efficiency) absorption comparison spectra for the standard and PFPAI treated devices (200, 500, and 1000 mM).

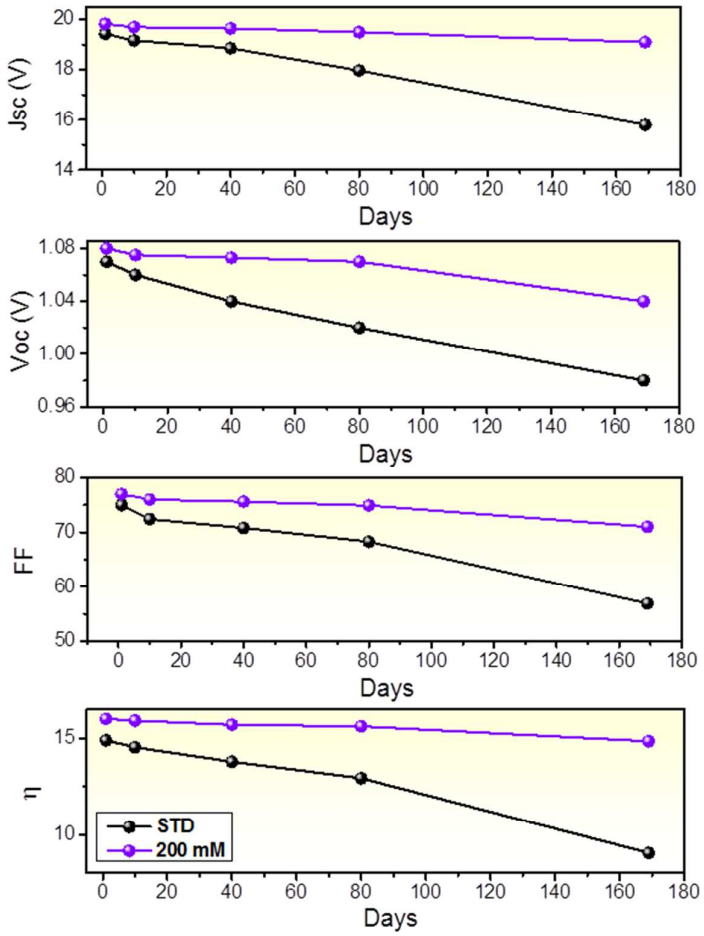

Figure S10. The overall aging data (over 80 days) for the device parameters like a) Jsc, b) Voc, c) FF, and d) PCE. All the devices were kept in a dry cabinet (with a relative humidity of 50 %) in the dark and measured in the ambient atmosphere under 100 mW cm^{-2} AM 1.5G simulated solar light.

Table S3. Arbitrary Parameters used to fit the TPRL curves for the standard, 200 mM, 500 mM, and 1000 mM perovskite films. The perovskite films were prepared on glass substrates. The PL decay curves, $P(t)$ were fitted using an empirical biexponential equation; given below as equation (1)

$$P = A_1 \exp(-t/\tau_1) + A_2 \exp(-t/\tau_2) + C \quad \ldots\ldots\ldots\ldots\ldots\ldots (1)$$

Where A_1 and A_2 are the relative amplitudes and τ_1 and τ_2 are the best-fit PL decay times.

Sample	A_1	τ_1 (ns)	A_2	τ_2 (ns)	$\langle\tau_{avg}\rangle^a$ (ns)
STD	0.90	183.19	0.10	6.74	165
200 mM	0.86	196.57	0.14	6.66	170
500 mM	0.81	163.80	0.19	7.61	134
1000 mM	0.61	120.15	0.39	7.99	76

[a]$\langle\tau_{avg}\rangle$ is the average life time; $\langle\tau_{avg}\rangle = (A_1*\tau_1) + (A_2*\tau_2)/ (A_1+A_2)$, whereas $(A_1+A_2) = 1$.

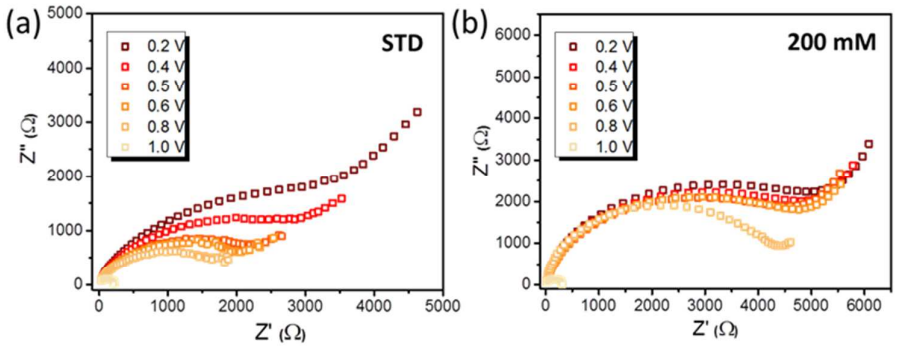

Figure S11. Bias-dependent Nyquist plot of the a) standard and b) 200 mM modified devices under dark (at 0.2 V, 0.4 V, 0.5 V, 0.6 V, 0.8 V, and 1 V) condition.

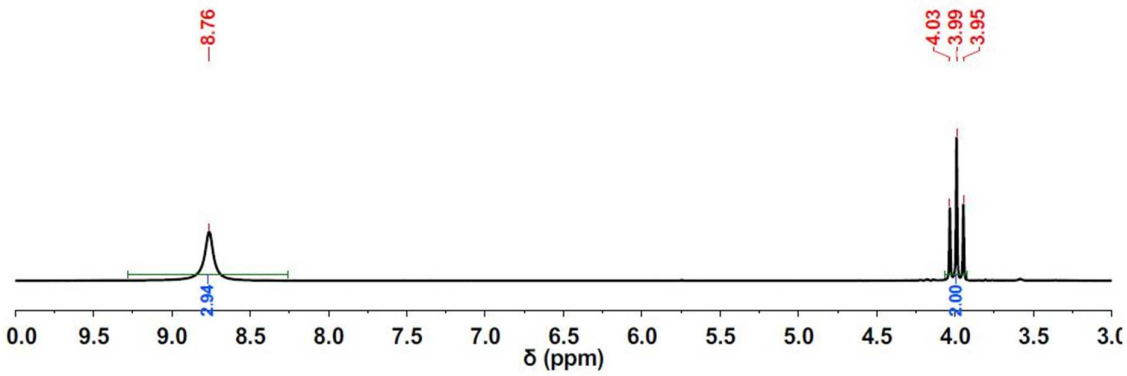

Figure S12. ^{1}H NMR of 2,2,3,3,3-pentafluoropropyl ammonium iodide (PFPAI) in DMSO-d6

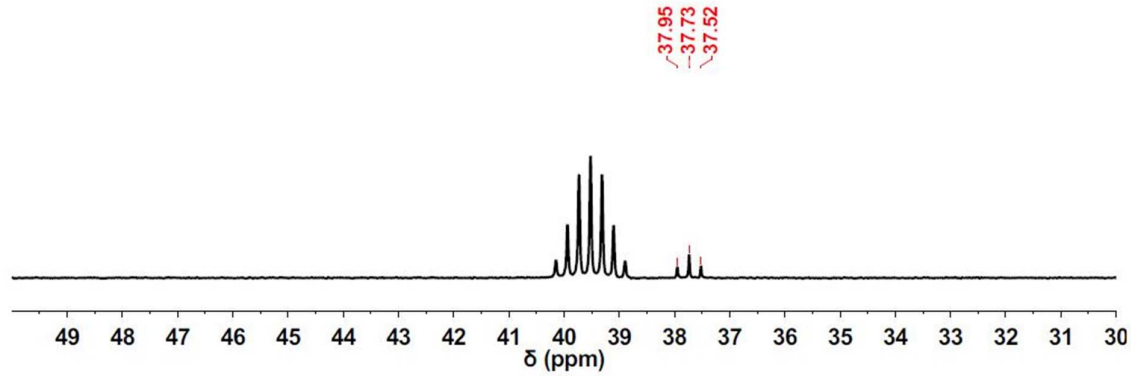

Figure S13. ^{13}C NMR of 2,2,3,3,3-pentafluoropropyl ammonium iodide (PFPAI) in DMSO-d6

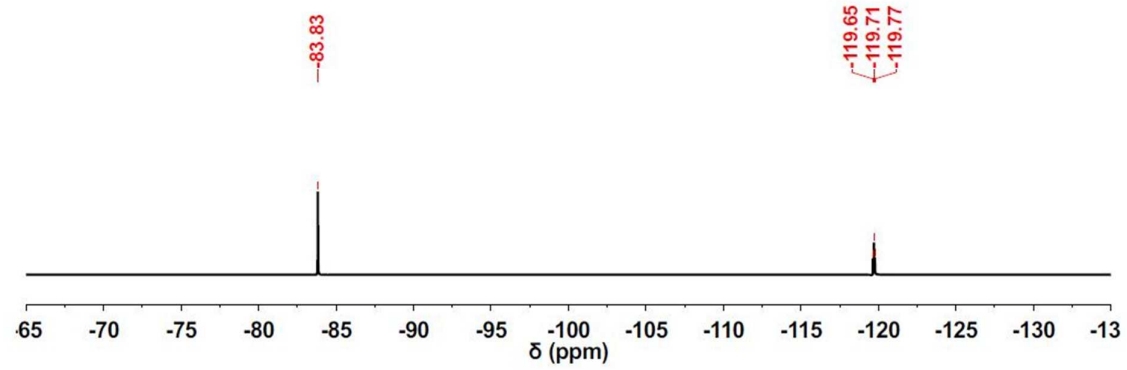

Figure S14. ^{19}F NMR of 2,2,3,3,3-pentafluoropropyl ammonium iodide (PFPAI) in DMSO-d6

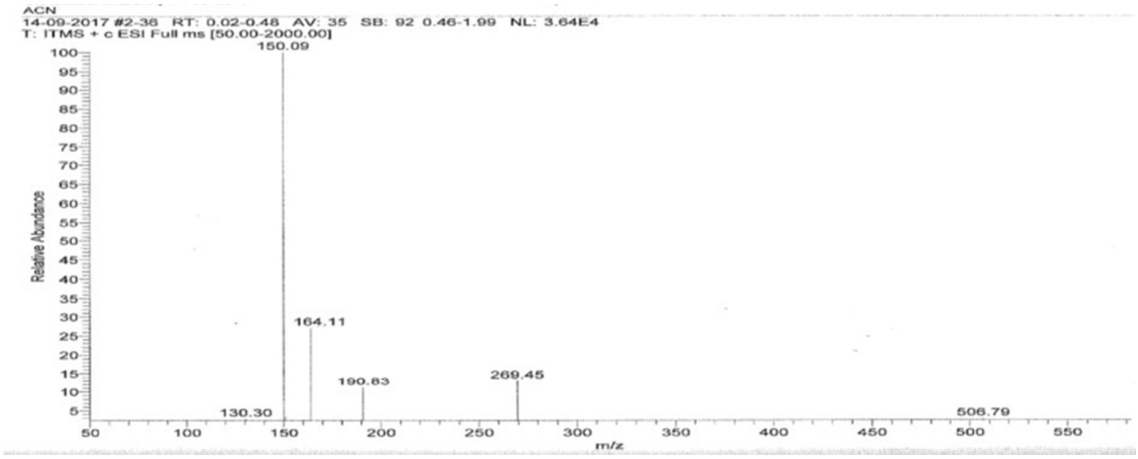

Figure S15. Mass Spectrum (EI, 70 eV) of 2,2,3,3,3-pentafluoropropyl ammonium iodide (PFPAI) in Acetonitrile, showing m/z of 150.09 (M^+).

References

1. Saliba, M.; Matsui, T.; Seo, J.-Y.; Domanski, K.; Correa-Baena, J.-P.; Nazeeruddin, M. K.; Zakeeruddin, S. M.; Tress, W.; Abate, A.; Hagfeldt, A. Cesium-Containing Triple Cation Perovskite Solar Cells: Improved Stability, Reproducibility and High Efficiency. *Energy Environ. Sci.* **2016**, *9* (6), 1989-1997.